Supporting Information

Carrier Management via Integrating InP Quantum Dots into Electron Transport Layer for Efficient Perovskite Solar Cells

*Jinpeng Wu[1, 2], Ming-Hua Li[1], Yan Jiang[3, *] Qiaoling Xu[3, 4], Lede Xian[3, 5], Haodan Guo[1, 2], Jing Wan[1, 2], Rui Wen[1, 2], Yanyan Fang[1, 2], Dongmei Xie[1, 2], Yan Lei[1, 2, *] Jin-Song Hu[1, 2, *] and Yuan Lin[1, 2, *]*

[1] Beijing National Laboratory for Molecular Sciences, Institute of Chemistry, Chinese Academy of Sciences

Beijing 100190, China

[2] School of Chemical Sciences, University of Chinese Academy of Sciences, Beijing 100049, China

[3] Songshan Lake Materials Laboratory, Dongguan 523808, Guangdong, China

[4] College of Physics and Electronic Engineering, Center for Computational Sciences, Sichuan Normal University, Chengdu 610068, China

[5] Max Planck Institute for the Structure and Dynamics of Matter, Center for Free Electron Laser Science, 22761 Hamburg, Germany

*Corresponding Authors: jiangyan@sslab.org.cn (Y. Jiang); leiyan@iccas.ac.cn (Y. Lei); hujs@iccas.ac.cn (J. Hu); linyuan@iccas.ac.cn (Y. Lin).

Conductivity measurements. The electrical conductivities (σ) of the ETL films can be determined with the following formula (1):[1]

$$\sigma = \frac{G_0 d_0}{A} \quad (1)$$

where G_0 is the conductance calculated from the slope of the $I-V$ curves, d_0 is the film thickness of ETLs, and A is the effective areas.

Electron mobility measurements

The electron mobility (μ_e) of the SnO_2 and hybrid InP CQDs-based ETLs were estimated by the space charge limited current (SCLC) method with the electron-only device ITO/ETL/PCBM/Au.[2] *J-V* curves were fitted according to the SCLC model using the Mott-Gurney Equation (2):

$$J = \frac{9\varepsilon_0\varepsilon_r\mu(V_{bias}-V_{bi})^2}{8L^3} \quad (2)$$

Here, J is the dark current density, ε_0 is the permittivity of the vacuum (8.854×10^{-12} F m^{-1}), ε_r is the relative permittivity which is assumed to be a typical value of 9 for inorganic semiconductor,[3] V_{bias} is the applied voltage, V_{bi} corresponds to the built-in voltage, and L (40 nm) is the thickness of the film.

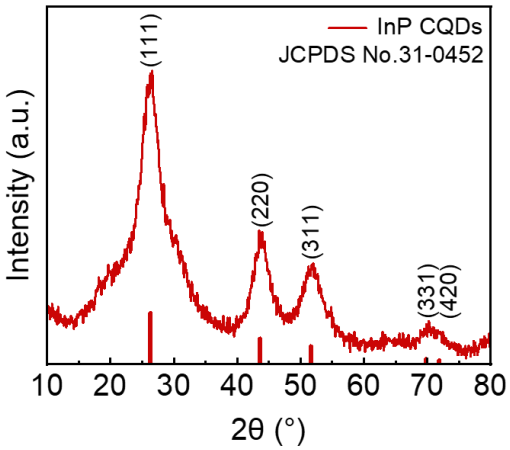

Figure S1. X-ray diffraction pattern of water-soluble InP CQDs. The diffraction peaks can be well indexed with the cubic phase InP (space group F43/mnm, a = 0.5869, JCPDS#31-0452).

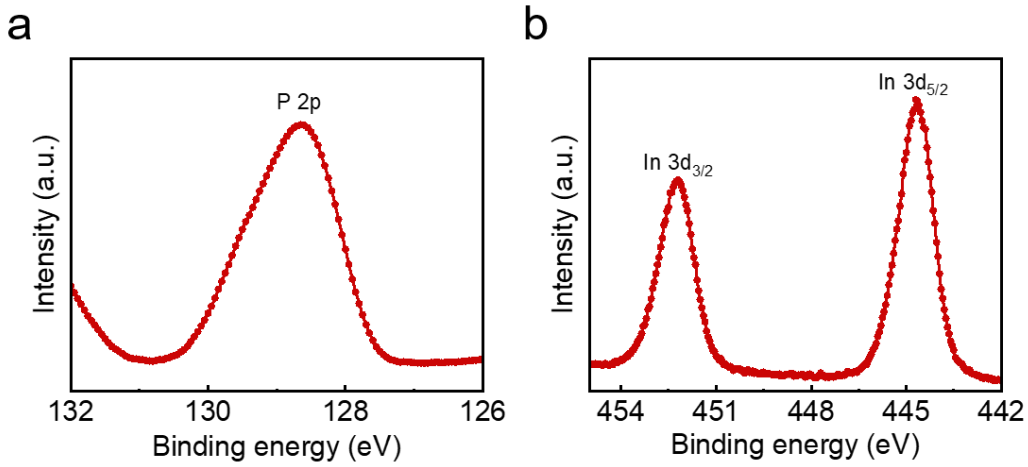

Figure S2. XPS of InP CQDs film deposited on Si substrate. (a) P 2p core level and (b) In 3d core-level spectra of InP CQDs films.

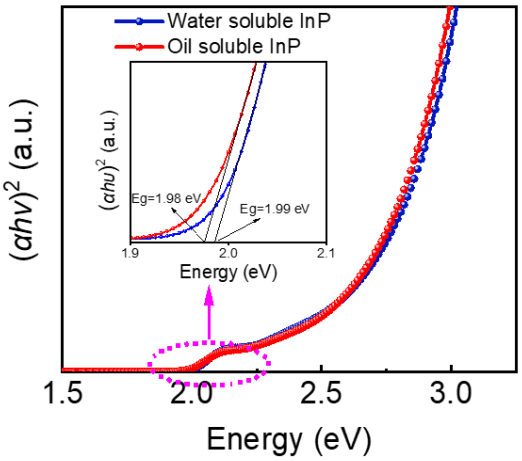

Figure S3. The calculated bandgaps of oil-soluble and water-soluble InP CQDs. The bandgaps of two samples were determined by the point of intersection of the linear extrapolation of the $(\alpha h\mu)^2$ curves and the horizontal axis.

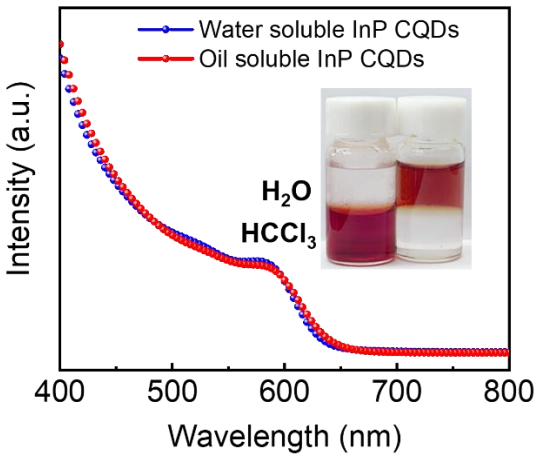

Figure S4. UV–vis absorption spectra of oil-soluble and water-soluble InP CQDs. The inset shows a photograph of InP CQDs dissolved in chloroform and deionized water.

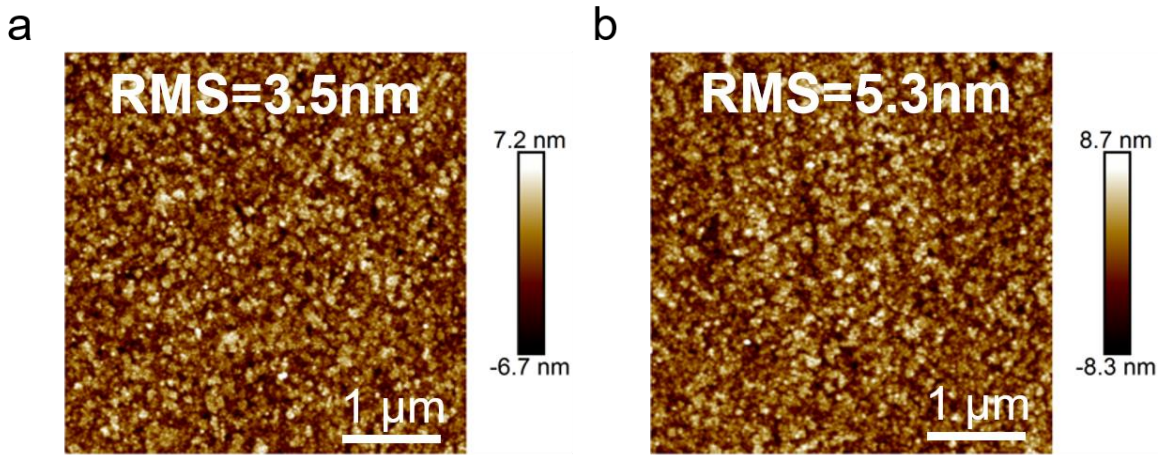

Figure S5. Surface roughness of (a) hybrid InP CQDs-based ETL and (b) SnO_2 films.

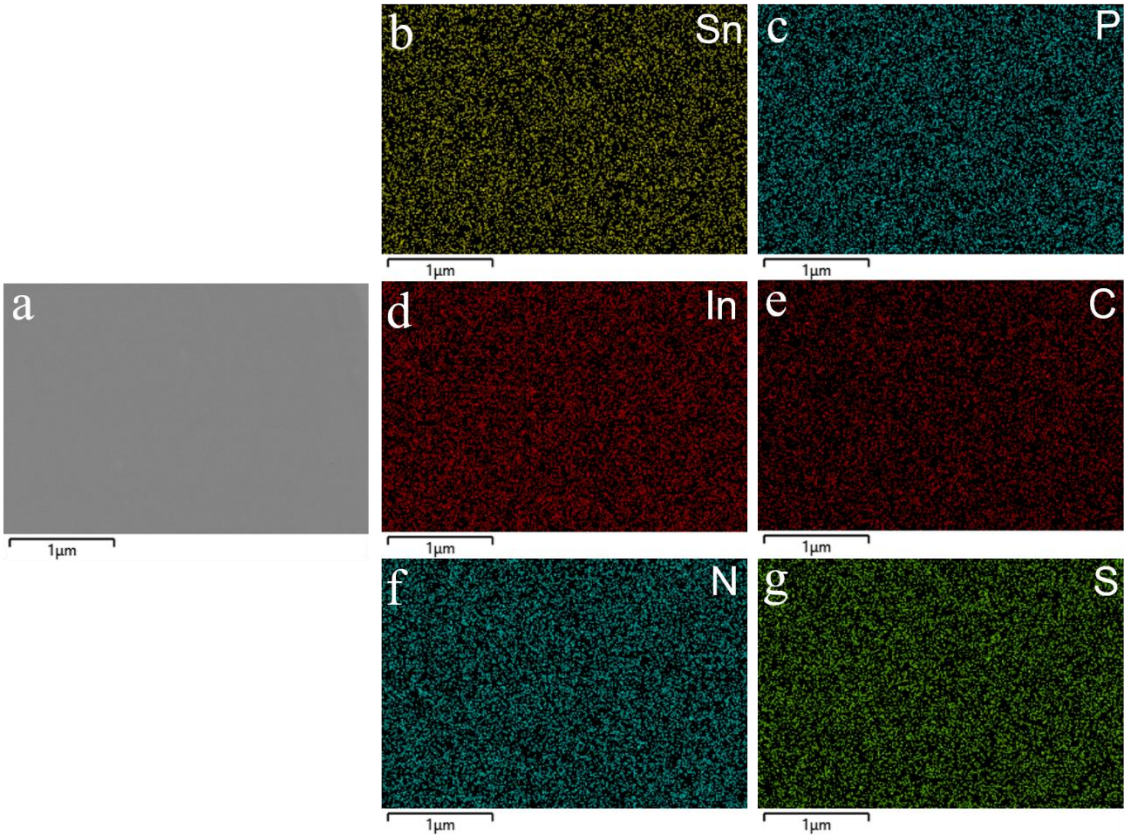

Figure S6. SEM (a) and the corresponding (b-g) EDS mapping images of a hybrid InP CQDs-based film. The scale bar is 1 μm. The Sn, P, In, C, N and S elements are uniformly distributed across the ETL thin film. It should be noted that the above EDS signals of elements N and S come from the organic ligand dithiocarbamate moieties.

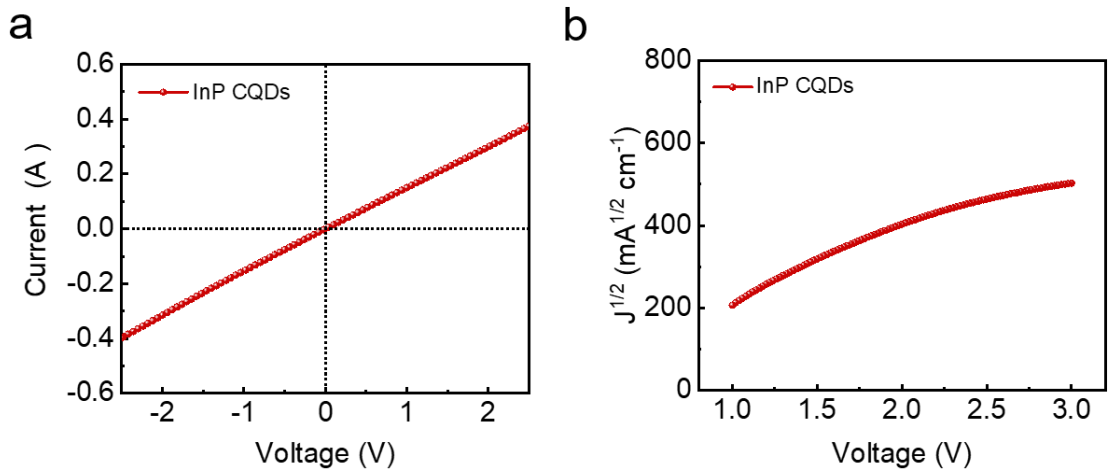

Figure S7. (a) Conductivity and (b) electron mobility of InP CQDs.

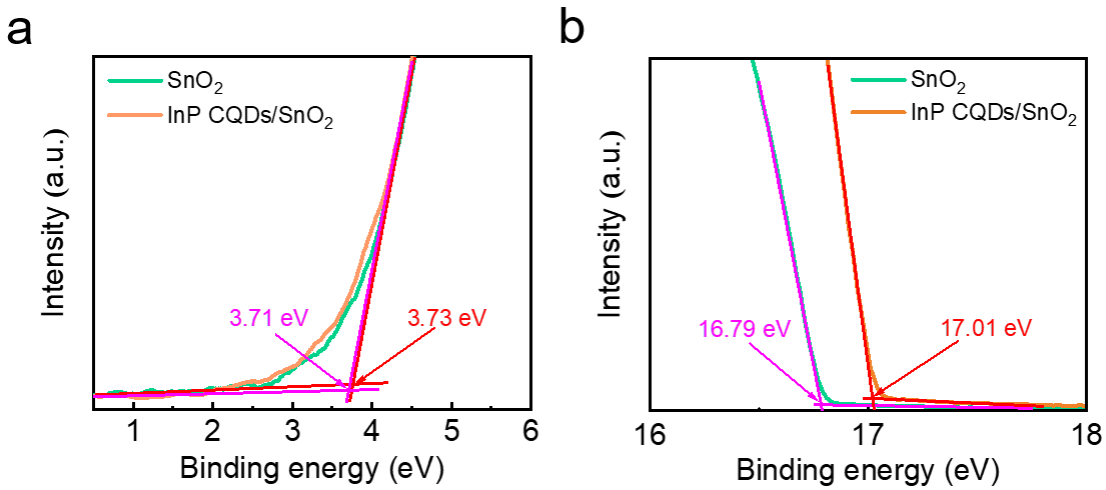

Figure S8. Ultraviolet photoelectron spectroscopy (UPS) (a) valence band spectra and (b) cutoff edge of SnO_2 and hybrid InP CQDs-based ETLs.

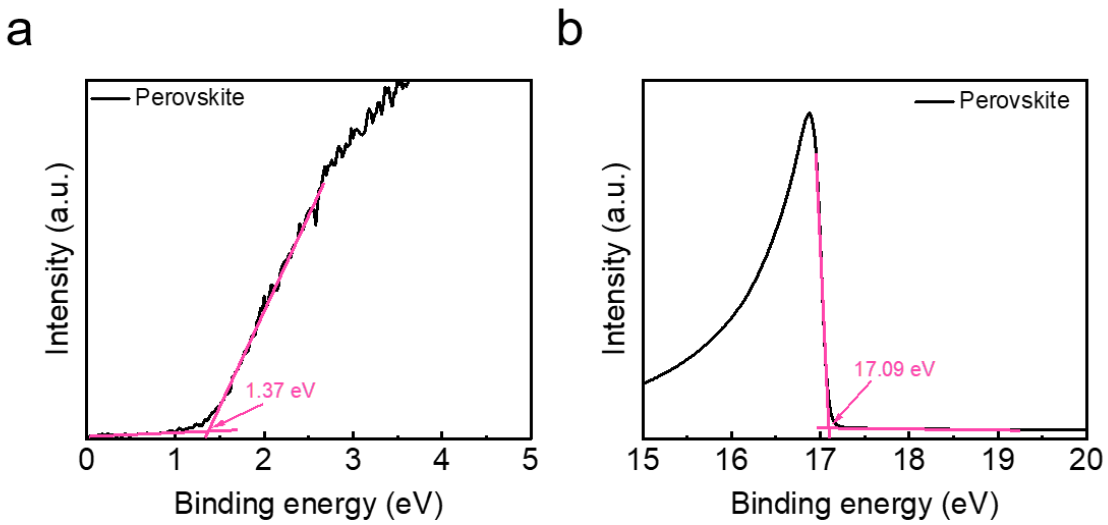

Figure S9. UPS (a) valence band spectra and (b) the cutoff edge of perovskite.

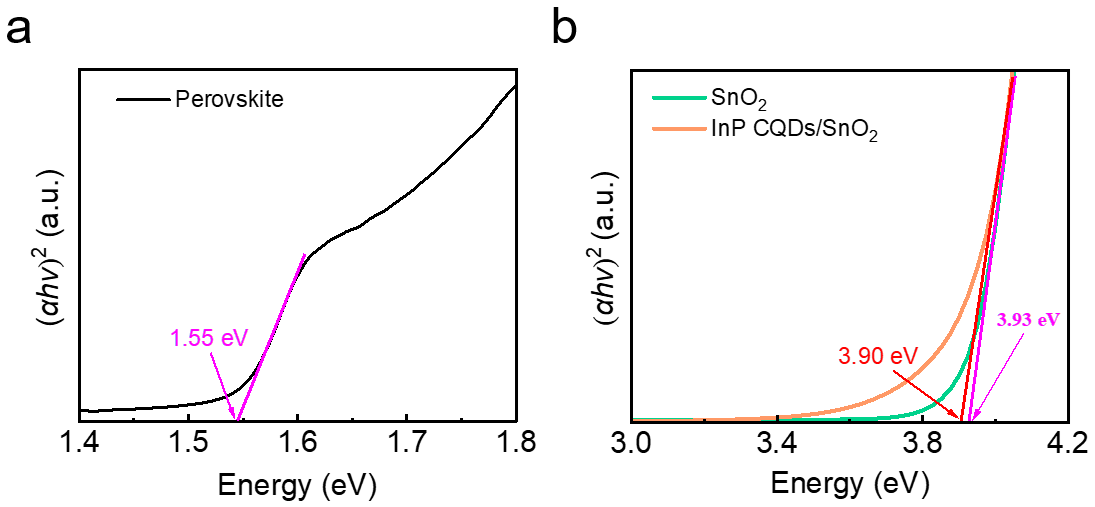

Figure S10. The relationship of $(\alpha h\mu)^2$ vs. energy of (a) perovskite, (b) SnO_2 and hybrid InP CQDs-based films. Bandgaps of perovskite, SnO_2 and hybrid InP CQDs-based ETLs are 1.55 eV, 3.93 eV and 3.90 eV, respectively.

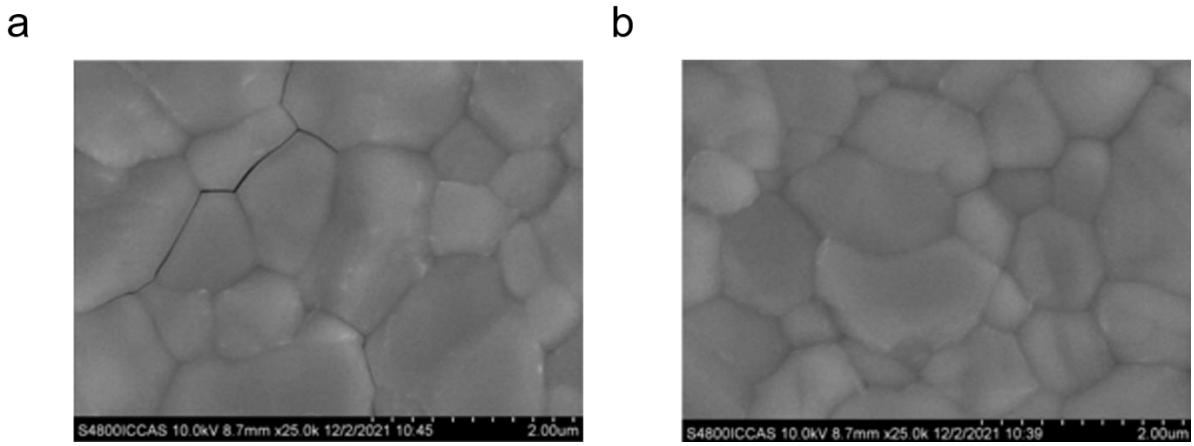

Figure S11. Top-view SEM images of perovskite films deposited on (a) SnO_2 and (b) hybrid InP CQDs-based ETLs.

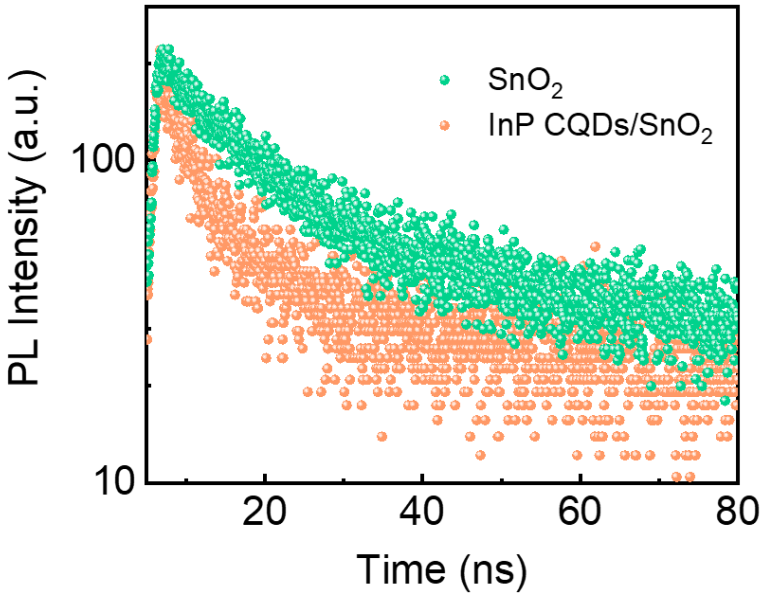

Figure S12. Time-resolved PL spectra of SnO_2/perovskite and InP CQDs/SnO_2/perovskite. The device architecture: ITO/ETL/perovskite. Lifetime values extracted from TRPL measurements conducted on a sample of perovskite/charge transport layer may be contributed from both the carrier recombination and extraction. Because the recombination and extraction processes occur at different time regimes, they can be distinguished. In our case, the TRPL spectra of perovskite/charge transport layer can be fitted by a biexponential decay function: $\tau = A_1 \exp(-t/\tau_1) + A_2 \exp(-t/\tau_2)$, with fast and slow decay lifetimes of τ_1 and τ_2. The slow decay lifetime τ_2 can be assigned to the carrier recombination process in the bulk region, while the fast lifetime τ_1 represents a charge-transfer process at the interface.[4] Lifetimes of SnO_2 samples are 7.76 ns (τ_1) and 49.99 ns (τ_2), respectively, which are larger than 6.94 ns (τ_1) and 26.21 ns (τ_2) of InP CQDs/SnO_2 samples. This means that the carrier recombination process is suppressed and the carrier transfer process is promoted.

Table S1. The TRPL parameters extracted from Figure S12, fitted by bi-exponential function of $y = y_0+A_1\exp(-t/\tau_1) + A_2\exp(-t/\tau_2)$.

Devices	**A_1**	**τ_1 [ns]**	**A_2**	**τ_2 [ns]**	**τ_{ave} [ns]**
SnO_2	36.11	7.76	63.89	49.99	46.58
InP CQDs/SnO_2	36.00	6.94	64.00	26.21	23.71

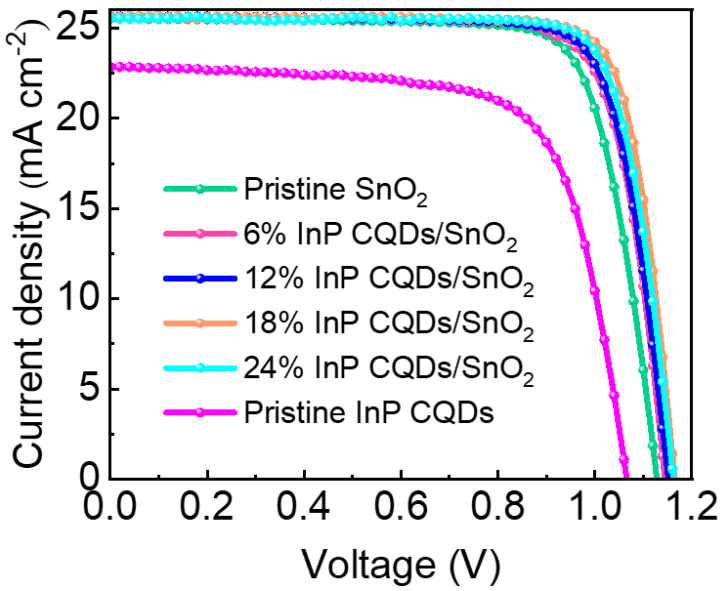

Figure S13. *J*–*V* curves of the PSCs with different ETLs.

Table S2. InP CQDs concentration-dependent *J*-*V* curves. All the device structure and fabrication procedures were the same except for the InP concentration.

Devices	V_{oc} (V)	J_{sc} (mA cm^{-2})	*FF* (%)	PCE (%)
SnO_2	1.128	25.53	77.72	22.38
6% InP CQDs/SnO_2	1.144	25.57	78.67	23.01
12% InP CQDs/SnO_2	1.152	25.64	79.30	23.42
18% InP CQDs/SnO_2	1.165	25.70	80.47	24.09
24% InP CQDs/SnO_2	1.161	25.60	80.18	23.83
InP CQDs	1.065	22.85	70.36	17.12

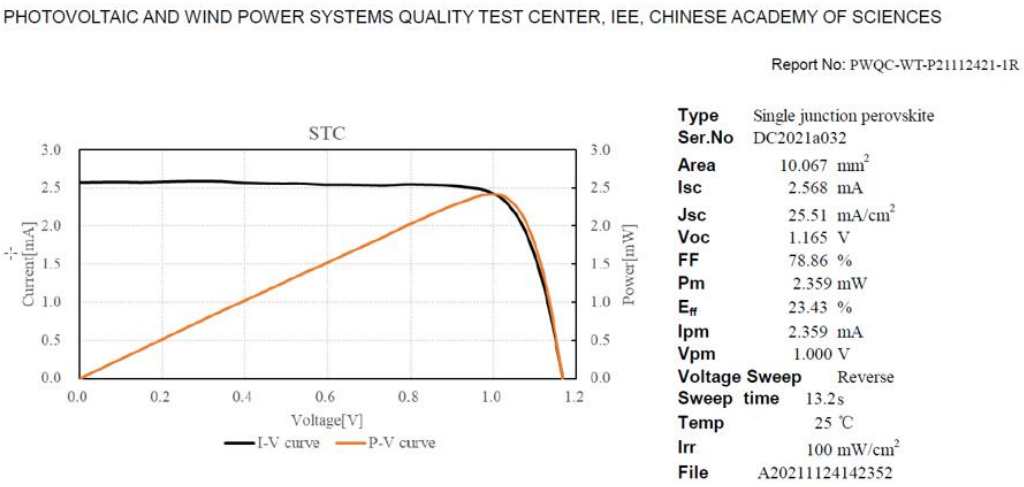

Figure S14. Certification of PSC efficiency (Institute of Electrical Engineering Chinese Academy of Sciences for certification). The PSC with the hybrid InP CQDs-based ETL exhibits a PCE of 23.43%.

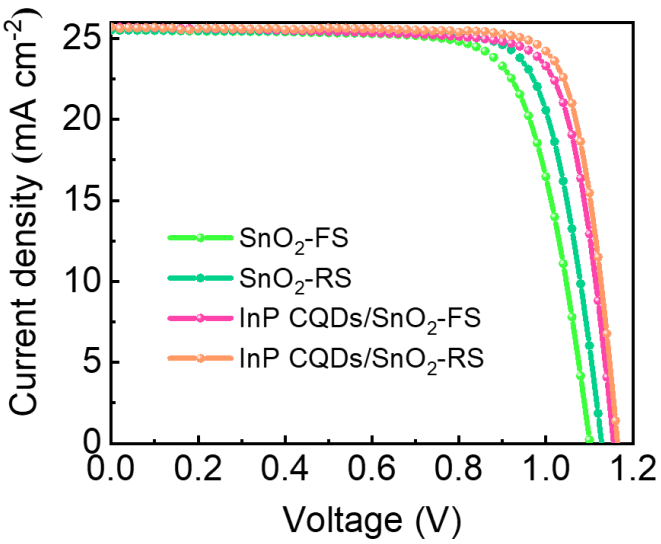

Figure S15. *J*–*V* curves of the PSCs based on SnO_2 and hybrid InP CQDs-based ETLs recorded from forward and reverse scans.

Table S3. Photovoltaic parameters of *J*-*V* curves in Figure S15.

Devices	Scan mode	V_{oc} (V)	J_{sc} (mA cm^{-2})	*FF* (%)	PCE (%)	HI index (%)
SnO_2	Reverse	1.128	25.53	77.72	22.38	5.81%
	Forward	1.102	25.52	74.98	21.08	
InP CQDs /SnO_2	Reverse	1.165	25.70	80.47	24.09	2.78%
	Forward	1.156	25.70	78.83	23.42	

The hysteresis index (HI) is calculated according to the formula HI = ($PCE_{reverse}$ - $PCE_{forward}$) / $PCE_{reverse}$ × 100%.

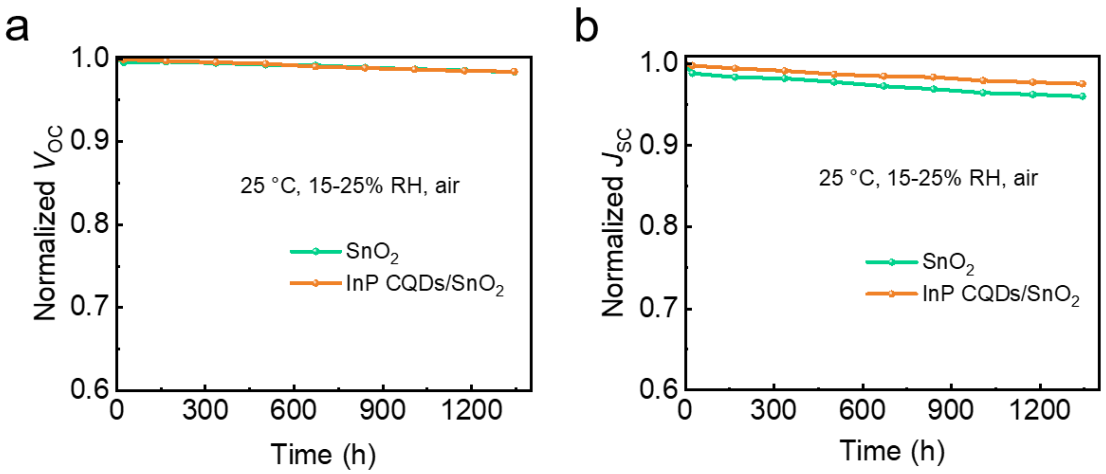

Figure S16. Normalized (a) V_{oc} and (b) J_{sc} as a function of time for the devices with pristine SnO_2 and hybrid InP CQDs-based ETLs.

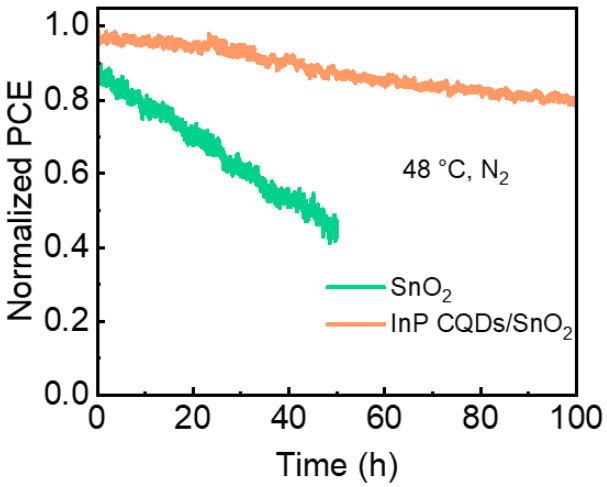

Figure S17. Operational stability of SnO_2 and hybrid InP CQDs-based PSCs without encapsulation under continuous illumination (100 mW cm^{-2}) at maximum power point (MPP) in a N_2 glovebox. The devices reached 48 °C during the test.

References

(1) Zhang, J.; Li, R.; Apergi, S.; Wang, P.; Shi, B.; Jiang, J.; Ren, N.; Han, W.; Huang, Q.; Brocks, G.; Zhao, Y.; Tao, S.; Zhang, X. Multifunctional Molecule Engineered SnO_2 for Perovskite Solar Cells with High Efficiency and Reduced Lead Leakage. *Solar RRL* **2021**, *5* (10), 2100464.

(2) Yuan, R.; Cai, B.; Lv, Y.; Gao, X.; Gu, J.; Fan, Z.; Liu, X.; Yang, C.; Liu, M.; Zhang, W.-H. Boosted Charge Extraction of NbO_x-Enveloped SnO_2 Nanocrystals Enables 24% Efficient Planar Perovskite Solar Cells. *Energy Environ. Sci.* **2021**, *14* (9), 5074-5083.

(3) van Daal, H. J. The Static Dielectric Constant of SnO_2. *J. Appl. Phys.* **1968**, *39* (9), 4467-4469.

(4) Jiang, T.; Chen, Z.; Chen, X.; Chen, X.; Xu, X.; Liu, T.; Bai, L.; Yang, D.; Di, D.; Sha, W. E. I.; Zhu, H.; Yang, Y. M. Power Conversion Efficiency Enhancement of Low-Bandgap Mixed Pb−Sn Perovskite Solar Cells by Improved Interfacial Charge Transfer. *ACS Energy Lett.* **2019,** *4*, 1784-1790.